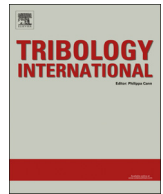




ELSEVIER

Contents lists available at ScienceDirect

Tribology International

journal homepage: www.elsevier.com/locate/triboint

Loading–unloading normal stiffness model for power-law hardening surfaces considering actual surface topography



Bin Zhao, Song Zhang*, Peng Wang, Yuan Hai

Key Laboratory of High Efficiency and Clean Mechanical Manufacture (Ministry of Education), School of Mechanical Engineering, Shandong University, 17923 Jinan Road, PR China

ARTICLE INFO

Article history:

Received 14 January 2015

Received in revised form

24 April 2015

Accepted 28 April 2015

Available online 8 May 2015

Keywords:

Normal stiffness

Power-law hardening

Shoulder–shoulder contact

Surface topography

ABSTRACT

Contact surfaces widely exist in the engineering applications and their contact behaviors strongly affect the mechanical performance. The normal contact stiffness, as an important contact parameter, is studied during loading and unloading process. The normal stiffness of single asperity contact is calculated based on the contact between a power-law hardening hemisphere and a rigid flat under full stick condition and the shoulder–shoulder contact form. The actual surface topography is considered efficiently to build the stiffness model of contact surfaces. The stiffness predicted by the proposed model is verified by the experiments.

© 2015 Elsevier Ltd. All rights reserved.

1. Introduction

Contact is ubiquitous in engineering applications, such as MEMS [1], head–disk interface [2], connectors [3], gears [4] and so on. The contact behaviors have great influence on friction [5], wear [6], and conduction of heat and electricity [7]. As one of the important parameters affecting contact behavior, contact stiffness needs to be studied in detail. However, all actual surfaces are rough on a microscopic scale and consist of asperities having different radii and heights. When they are compressed together, the contact is discontinuous and only occurs at discrete points. Consequently, the contact force and deformation vary nonlinearly and the mechanism of the contact stiffness is extremely complicated.

Two approaches are commonly used to explore the stiffness. One is the experimental approach, where the stiffness can be identified utilizing novel techniques such as ultrasonic assessment [8], digital image correlation [9], modal analysis [10] and virtual fields method [11]. The other approach is to build the theoretical contact model and derive the contact stiffness further. There are several kinds of contact models, e.g. statistics model, deterministic model, fractal models and finite element (FE) models. The statistics model was proposed originally by Greenwood and Williamson [12], and improved by many subsequent researchers [13–15]. The deterministic model [16,17] considered all actual geometrical characteristics of the asperities on contact surfaces. The concept

of fractals was presented by Mandelbrot [18], and was introduced to describe surfaces and to build the fractal models [19–21] later. By comparison, the FE model is more precise to study single asperity contact which is the base of the surfaces contact. Kogut and Etsion [22] provided an accurate solution to study the contact between an elastic–plastic sphere and a rigid flat. They concluded that the evolution of the contact could be divided into three distinct stages ranging from elastic to plastic, and proposed empirical equations to calculate the contact parameters (contact force and contact area) which were negligibly affected by the ratio of Young's modulus to yield strength E/Y_0 . Jackson and Green [23] provided a more accurate FE model with finer meshes and acquired another generalized expressions for contact parameters. They concluded contact parameters were affected by the deformed contact geometry. Shankar and Mayuram [24] studied the effect of the yield strength and the tangent modulus on the transition behaviors of materials from elastic–plastic to the fully plastic case. They derived new empirical relations of the contact parameters and validated them with an experiment. However, these FE models [22–24] only dealt with the loading case but neglected the unloading process. Actually, unloading also plays an important role in many applications, such as MEMS micro switches [25], head–disk interaction in magnetic storage systems [26] and so on. Etsion et al. [27] studied the unloading process of an elastic–plastic loaded sphere in contact with a rigid flat. They gave the dimensionless expressions for the unloading load–deformation relation and the residual interference after complete unloading. This expression was generalized and independent of specific materials or radii of the sphere. Kadin et al. [28] improved this model to consider the effect of adhesion during unloading. Jackson

* Correspondence to: School of Mechanical Engineering, Shandong University, 17923 Jingshi Road, Jinan 250061, PR China Tel./fax: +86 53 188 392 746.

E-mail address: zhangsong@sdu.edu.cn (S. Zhang).

Nomenclature

A	contact area	R	radius of the hemisphere
A_c	critical contact area at yielding inception	R_s	sum of radii of summits of asperity on surface 1 and 2
A_{\max}	maximum contact area before unloading	$R_{v,1}, R_{v,2}$	radii of summits of asperity on surface 1 and 2
A^*	dimensionless contact area	$R_{v,1}(r), R_{v,2}(r)$	radii at the contact point of asperity on surface 1 and 2
A_{\max}^*	dimensionless maximum contact area	$R_{v,s}(r)$	equivalent asperity radius at contact point
a	contact radius	r	tangential offset of two contact asperities
d	mean separation of two surfaces	S	nominal contact area
E	Young modulus of the hemisphere	w	contact interference
E'	combined Young's modulus of two materials	w_1	interference defined in Greenwood and Tripp
E_T	tangent modulus of the hemisphere	w_c	critical interference at yielding inception
F_n	normal force of contact surfaces	w_{\max}	maximum contact interference before unloading
f	contact force	w_{res}	residual contact interference after fully unloading
f_c	critical load at yielding inception	w^*	dimensionless contact interference
f_{\max}	maximum contact force	w_{\max}^*	dimensionless maximum contact interference
f_n^L	normal components of contact force during loading	w_{res}^*	dimensionless residual contact interference after fully unloading
f_n^U	normal components of contact force during unloading	Y_0	virgin yield strength of the hemisphere
f_n^*	dimensionless contact force	z_1, z_2	heights of summits of asperity on surface 1 and 2
f_n^{*L}	dimensionless contact force in loading process	α	contact angle
f_n^{*U}	dimensionless contact force in unloading process	δ_n	change of normal relative deformation of asperities
K_n	normal stiffness of contact surfaces	η	asperity density
k_n^L	normal stiffness in loading process	λ	error between theoretical models and experiments
k_n^U	normal stiffness in unloading process	μ_x	average value of $x, x=E, Y_0, \nu, n; R, z, \eta$
n	strain hardening exponent	ν	Poisson's ratio
P	normal pressure of contact surfaces	σ_x	standard deviation of $x, x=E, Y_0, \nu, n; R, z, \eta$
K_n	normal stiffness of contact surfaces	ψ	plasticity index of contact materials

[29] studied the residual stress and deformation in hemispherical contacts during loading and unloading. Jackson [30] predicted the residual deformation of impacting elastic-perfectly plastic spheres during unloading.

Almost all the above FE models were built on the assumed frictionless contact condition. Nevertheless, friction widely exists in the practical applications and the frictionless assumption has been proved invalid in dry contact of dissimilar materials experimentally by McGuiggan [31] and Ovcharenko et al. [32]. Recently, full stick condition was employed in many studies. Brizmer et al. [33,34] analyzed the effect of two contact conditions (frictionless and full stick) on the elasticity terminus and the elastic-plastic properties of a spherical contact, and compared contact parameters under these two conditions. They found contact parameters were not much sensitive to contact conditions and were independent of the ratios E/Y_0 , but they were affected by Poisson's ratio ν . The contact area and the mean contact pressure showed good correlation with the experimental results given by Ovcharenko et al. [35]. Zait et al. [36] studied the unloading process of a spherical contact under full stick condition, and proposed the residual profile of the sphere and residual von Mises stresses within the sphere. The theoretical results accorded well with the experiments.

It can be seen from the literature review that many contact models have been developed and modified recently. However, some problems still should be improved further. First, all the aforementioned FE models investigated the contact between a rigid flat and a linear hardening sphere with tangent modulus as 2% of Young's modulus. But power-law materials [37–39] are rarely considered, whose hardening law is more appropriate to be described by power function. And the contact stiffness for power-law hardening materials is an important parameter to study the static and dynamic characteristics of the mechanical equipment made of this kind of materials. Secondly, many FE

models simplified the asperity contact as the contact between a rigid flat and a sphere. In this work, considering many asperities were in contact with others obliquely, a shoulder-shoulder asperity contact form [40] was employed. Finally, to investigate the contact of rough surfaces, many models employed a statistical description of rough surfaces [41], or special sinusoidal surfaces [42], or other incomplete description of the real topographies with the same summit radii [43]. By comparison, the deterministic method could describe the surface contact more accurately, as they considered the asperity locations and actual geometry parameters more completely.

In this study, a normal stiffness model for power-law hardening surfaces during loading and unloading process is proposed. The contact model of a single asperity pair is built at first, based on the contact between a power-law hardening hemisphere and a rigid flat under stick condition. Then a modified shoulder-shoulder asperity contact form is employed to establish the stiffness model of single asperity contact. To consider the effect of the actual surface details, the locations and geometrical characteristics of asperities of real metallic specimens are analyzed, with which the asperities are generated to simulate the real contact between surfaces. After that, the stiffness of contact surfaces is derived by summing the components of each single asperity pair. The predicted results are testified by the experiments.

Two hypotheses are taken for simplification in this work: (i) the asperities are in contact with each other independently, and (ii) the deformation of substrate which the asperities attach to is ignored.

2. Contact model of a single asperity pair

The model is built on the contact between a power-law hardening hemisphere and a rigid flat under full stick condition,

considering the effect of the strain hardening exponent n and Poisson's ratio ν .

2.1. Power-law hardening property

The hemisphere material is assumed to be elastic–plastic, whose plastic behavior obeys the J_2 flow theory and satisfies a power hardening law reconstructed by the classical Ramberg–Osgood curve [37]. The relation of the strain ε to the stress τ for power-law hardening materials is given as

$$\tau = \begin{cases} E\varepsilon, & \tau \leq Y_0 \\ Y_0((E/Y_0)\varepsilon)^n, & \tau > Y_0 \end{cases} \quad (1)$$

where Y_0 and E are the yield strength and Young's modulus of the hemisphere, respectively, and n is the strain hardening exponent varying from 0 to 1. For two extreme cases, $n=1$ means the elastic case, while $n=0$ means the elastic–perfectly plastic case.

2.2. Finite element model

As shown in Fig. 1, a two-dimensional FE model was developed with the software ANSYS 14.0. The contact occurs between a rigid flat represented by a line and a deformable hemisphere modeled as a quarter of a circular plane whose radius is R . The quarter circular plane was divided into two zones: zone I within a $0.1R$ distance from the hemisphere tip was of most interest and had extremely fine mesh, while zone II outside the $0.1R$ distance was meshed coarsely. The hemisphere was discretized by eight-node PLANE183 elements. The contact was simulated with the two-dimensional surface-to-surface contact element (CONTA172) and a single nonflexible two-node target element (TARGE169). The resulting final mesh consisted of 13,750 of PLANE183 and 303 of CONTA172 elements.

Two boundary conditions are: (i) nodes on the symmetry axis are constrained to move only in the radial direction, and (ii) nodes at the bottom of the sphere cannot move in the axial direction due to symmetry [22]. Since it has been proved that the ratio E/Y_0 of the hemisphere has negligible effect on contact parameters [22,34], E/Y_0 was set as 500. Power-law was used to consider the hardening properties of the hemisphere, which is different from the line-hardening property in the model in reference [34]. An infinite friction condition was adopted to simulate the full stick contact condition, which is different from the frictionless condition in the model in reference [22]. The von Mises yielding criterion was employed to describe the transition from elastic to plastic. The augmented Lagrangian method was chosen as a solution method. This method has the same property as the penalty method where it reformulates the contact and friction conditions as a system of equations in contrast to inequalities, but contrary to the penalty method it involves no approximation of the original problem and is not subject to penalty sensitivity [44]. A displacement was applied to the rigid flat and the contact force could be calculated from the reaction forces of the nodes at the bottom of hemisphere.

To verify the accuracy of the FE model, the problems for different elastic material properties ($E/Y_0=500$, $0.2 \leq \nu \leq 0.4$, $n=1$) and sphere radii ($0.1 \text{ mm} \leq R \leq 10 \text{ mm}$) under frictionless condition were solved and tested against the Hertz solution [45]. The errors of the contact force were less than 1.7%. Moreover, to ensure mesh convergence, the mesh density was doubled iteratively until the results changed no more than 1% between successive iteration.

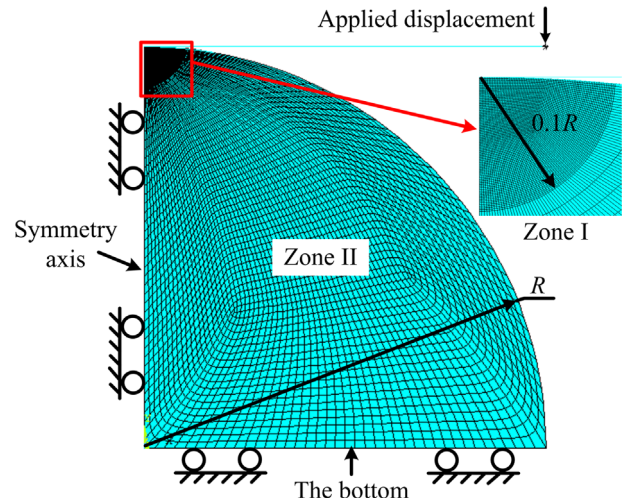


Fig. 1. The finite element model.

2.3. Numerical results

The loading and unloading process for the contact between a rigid flat and a deformable hemisphere has been studied by Brizmer et al. [33,34], Etsion et al. [27] and Kadin et al. [28]. However, they all focused on line hardening materials. In this work, the contact for the power law hardening materials is studied with the FE method based on their works [27,28,33,34], and the only difference is the material hardening law. The loading and unloading process was analyzed considering the effect of the strain hardening exponent n and Poisson's ratio ν . In this work, the relation of the contact force f to the interference w is most important to calculate the contact stiffness. The contact force and interference are normalized as f^* and w^* by the corresponding critical values f_c and w_c at yielding inception. The critical force and interference under stick condition are given by Brizmer et al. [33]:

$$f_c = \pi^3 Y_0 C_v^3 (R(1-\nu^2)(Y_0/E))^2 \times (8.88\nu - 10.13(\nu^2 + 0.089))/6 \quad (2)$$

$$w_c = (\pi C_v (1-\nu^2)(Y_0/E)/2)^2 \times R(6.28\nu - 7.83(\nu^2 + 0.0586)) \quad (3)$$

where C_v is a parameter which depends on Poisson's ratio ν as $C_v = 1.234 + 1.256\nu$.

In the loading process, the relations of the dimensionless contact force f_L^* versus the interference w^* were calculated for $\nu=0.2, 0.25, 0.3, 0.35$ and 0.4 at $n=0, 0.1, 0.2, 0.3, 0.4, 0.5, 0.6, 0.7, 0.8, 0.9$ and 1.0 . The range of interferences w^* is chosen from 0 to 150. For the sake of simplicity, only the results of $n=0.1, 0.4, 0.6$ and 0.9 for $\nu=0.2, 0.3$ and 0.4 are selected and shown in Fig. 2. The dimensionless relation of f_L^* versus w^* for line hardening materials was given by the Hertz solution [45] for the elastic case and by Brizmer et al. [34] for the elastic–plastic case as

$$f_L^* = \begin{cases} (w^*)^{3/2}, & w^* \leq 1 \\ (w^*)^{3/2}(1 - \exp(1/(1 - (w^*)^a))), & w^* > 1 \end{cases} \quad (4)$$

where $a = 0.174 + 0.08\nu$. In this work, the value of a was modified as a function of n and ν to make Eq. (4) apply to the contact between power law hardening materials. Then the function a was fitted with the FE results in the loading process in Fig. 2 by the least square method as follows:

$$a = -0.161n + 0.0723\nu + 0.184 \quad (5)$$

Adjusted R -square is used to assess the goodness of fit. The value above 0.90 means a good fit. Here the adjusted R -square of a was 0.986 by calculation, and the standard deviation of the fitting equation was 0.0046.

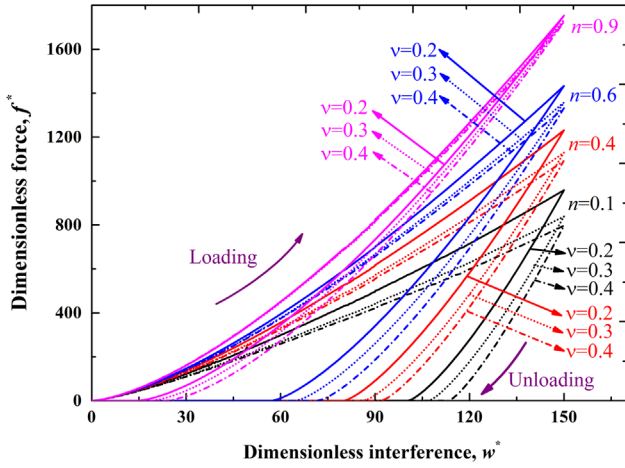


Fig. 2. The numerical results of the dimensionless contact force f^* versus the dimensionless interference w^* for hardening exponents n at 0.1, 0.4, 0.6, and 0.9 and Poisson's ratios ν at 0.2, 0.3, and 0.4 during the loading process where w^* varies from 0 to 150 and the subsequent unloading process from $w_{\max}^*/w_c = 150$.

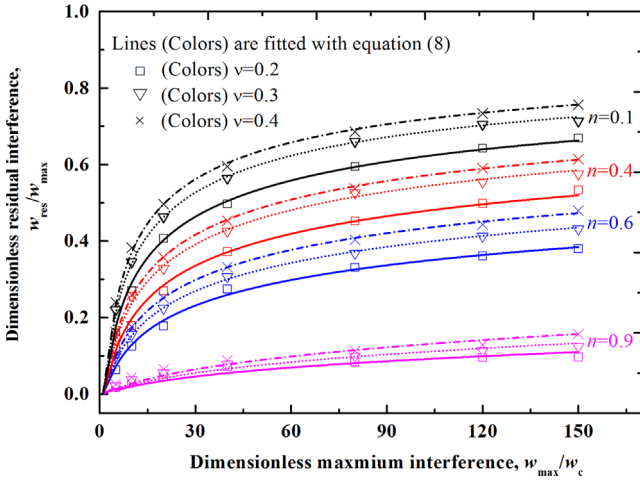


Fig. 3. The numerical results and fitting curves of the dimensionless residual interference $w_{\text{res}}^*/w_{\text{max}}^*$ versus the dimensionless maximum interference w_{max}^*/w_c at $w_{\text{max}}^*/w_c = 5, 10, 20, 40, 80, 120,$ and 150 for hardening exponents n at 0.1, 0.4, 0.6, and 0.9 and Poisson's ratios ν at 0.2, 0.3, and 0.4.

In the unloading process, since the unloading behavior is strongly affected by the maximal loading interference w_{\max} [27], the dimensionless relations of the contact force f_{U}^* versus the interference w^* for seven w_{\max}/w_c values of 150, 120, 80, 40, 20, 10 and 5 were analyzed at the same n and ν as those in the loading process. To show the results clearly, only the FE solutions unloaded from $w_{\max}/w_c = 150$ are displayed in Fig. 2. The empirical equations of f_{U}^* vs. w^* were obtained for line hardening materials by the Hertz solution [45] for the elastic case and by Etsion et al. [27] for the elastic–plastic case as

$$f_{\text{U}}^* = \begin{cases} (w^*)^{3/2}, & w^* \leq 1 \\ f_{\text{max}}^* ((w^* - w_{\text{res}}^*) / (w_{\text{max}}^* - w_{\text{res}}^*))^{1.5} (w_{\text{max}}^*)^b, & w^* > 1 \end{cases} \quad (6)$$

where $b = 0.0331$. For the contact between power law hardening materials in this study, b was modified as a function of n and ν by fitting the FE results in the unloading process in Fig. 2 as

$$b = 0.052n^2 + 0.071n\nu - 0.0405n - 0.0716\nu - 0.00591 \quad (7)$$

Adjusted R -square of b was 0.982 and the corresponding standard deviation of the fitting equation was 0.0017, demonstrating it is a good fit. w_{res}^* , w_{max}^* , and f_{max}^* are the dimensionless expressions of

the residual interference w_{res}/w_c , the maximal interference w_{max}/w_c and the maximal force f_{max}/f_c . The residual interference w_{res}^* for the given maximal interference w_{max}^* can be found after the contact force vanished (Fig. 3). The empirical expression for $w_{\text{res}}/w_{\text{max}}$ was founded for line hardening materials by Zait et al. [28]:

$$w_{\text{res}}/w_{\text{max}} = \left(1 - 1/(w_{\text{max}}/w_c)^c\right) \left(1 - 1/(w_{\text{max}}/w_c)^d\right) \quad (8)$$

where c and d were $c = 0.189\nu + 0.212$ and $d = -6.758\nu^2 + 5.281\nu - 0.308$. For the contact between power hardening materials, Eq. 8 was modified as follows:

$$w_{\text{res}}/w_{\text{max}} = \left(1 - 1/(w_{\text{max}}/w_c)^e\right)^2 \quad (9)$$

where e is a function of n and ν by fitting with the FE results in Fig. 3, which can be expressed as follows:

$$e = -0.112n^2 - 0.235n + 0.22\nu + 0.329 \quad (10)$$

Adjusted R -square is 0.991, which means this is an accurate fit.

3. Normal stiffness model of contact surfaces

As the contact of a single asperity pair is the foundation of the surfaces contact, thus the stiffness model of a single asperity pair should be established at first with the contact model presented in Section 2. However, several simplifications in this contact model were a bit idealistic which could be improved as follows: One was that the asperity shape could not be as regular as a hemisphere. By comparison, elliptic paraboloid is a more realistic asperity shape to ensure the contact area is elliptical. In addition, considering many asperities contact with others obliquely, a shoulder–shoulder asperity contact form [40] would be applied, with the elastic material replaced with the power-law hardening material in this work. The normal stiffness model was built on the contact model presented in Section 2 with these two modified assumptions above.

The shoulder–shoulder contact is illustrated in Fig. 4. The parameters are listed as follows: d is the mean separation of two surfaces; r is the tangential offset of two contact asperities; $R_{v,1}$ and $R_{v,2}$ are the radii of asperity summits and in contrast, $R_{v,1}(r)$ and $R_{v,2}(r)$ are those at the contact point; z_1, z_2 are the heights of summits; f means the contact force; α is the contact angle; w, w_1 are interferences in different directions. The expressions of w, w_1 and α are obtained by the geometric relationships

$$w = w_1 \cos \alpha \quad (11)$$

$$w_1 = z_1 + z_2 - d - r^2 / (2R_s) \quad (12)$$

$$\cos \alpha = (1 + r^2 / R_s^2)^{-0.5} \quad (13)$$

where $R_s = R_{v,1} + R_{v,2}$ is the sum of radii of summits.

The normal contact stiffness in the loading process, k_n^L , and in the unloading process, k_n^U , are the tangent to the curve $f_n = f_n^L(d)$ and $f_n = f_n^U(d)$, namely:

$$k_n^L = \partial f_n^L / \partial d, \quad k_n^U = \partial f_n^U / \partial d \quad (14)$$

where f_n^L and f_n^U are the normal components of contact force during loading and unloading, respectively. Thus the first task is to establish the relation between the contact force and the relative deformation, which has been accomplished preliminarily in Section 2. Nevertheless, for the assumed shoulder–shoulder contact form and the elliptic paraboloid asperity shape, some improvements and explanations should be added to modified the expressions of the critical contact force f_c and interference w_c in Eqs. (2) and (3). First, the hemisphere radius R should be replaced with the equivalent asperity radius at the

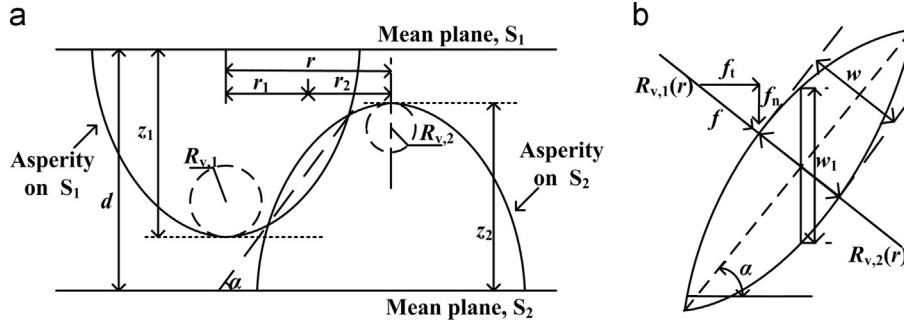


Fig. 4. Schematic of shoulder-shoulder asperity contact form (a) and overlap contact region which shows normal and tangential components of interferences and elastic-plastic forces (b).

contact point $R_{v,s}(r)$, whose expression was [40]:

$$R_{v,s}(r) = (1/R_{v,1} + 1/R_{v,2}) \left(1 + r^2/R_s^2\right)^{3/2} \quad (15)$$

Secondly, Young's modulus E should be replaced by combined Young's modulus E' of two contact materials, whose formula was

$$1/E' = (1 - \nu_1^2)/E_1 + (1 - \nu_2^2)/E_2 \quad (16)$$

where E_1 , E_2 and ν_1 , ν_2 are Young's moduli and Poisson's ratios of two contact surfaces, respectively. Finally, the Poisson's ratio ν in Eqs. (2) and (3) represents that of the softer contact material.

Compared with the expression of the force for the elastic contact in [40], the normal force of single asperity contact for power law hardening materials in loading process, f_n^L , was derived as follows:

$$f_n^L = f^L \cos \alpha = f_c^* f_c \cos \alpha = \begin{cases} (w^*)^{3/2} f_c (1 + r^2/R_s^2)^{-1/2}, & 0 < w^* \leq 1 \\ (w^*)^{3/2} f_c (1 - \exp(1/(1 - (w^*)^d))) (1 + r^2/R_s^2)^{-1/2}, & w^* > 1 \end{cases} \quad (17)$$

where f^L is the contact force during loading and a is the function given in Eq. (5). And the normal force in unloading process for power law hardening materials f_n^U was obtained similarly:

$$f_n^U = f^U \cos \alpha = f_c^* f_c \cos \alpha = \begin{cases} (w^*)^{3/2} f_c (1 + r^2/R_s^2)^{-1/2}, & 0 < w^* \leq 1 \\ (1 + r^2/R_s^2)^{-1/2} f_{\max} ((w^* - w_{\text{res}}^*) / (w_{\max}^* - w_{\text{res}}^*))^{1.5(w_{\max}^*)^b}, & w^* > 1 \end{cases} \quad (18)$$

where f^U is the contact force during unloading, and b is the function given in Eq. (7).

The normal stiffness of single asperity contact in loading and unloading process, k_n^L and k_n^U , were calculated by the general formula below together with Eqs. (11) and (12):

$$k_n = |\partial f_n / \partial d| = |(\partial f_n / \partial w_1) \times (\partial w_1 / \partial d)| = |(\partial f_n / \partial w) \cos \alpha| = |(\partial f_n / \partial w^*) \times (\partial w^* / \partial w) \cos \alpha| = |(\partial f_n / \partial w^*) \times (\cos \alpha / w_c)| \quad (19)$$

Substituting Eqs. (3), (13) and (17) into Eq. (19), the loading normal stiffness k_n^L was derived as

$$k_n^L = \begin{cases} 3(w^*)^{1/2} f_c (1 + r^2/R_s^2)^{-1} / (2w_c), & 0 < w^* \leq 1 \\ f_c (1 + r^2/R_s^2)^{-1} [1.5(w^*)^{1/2} (1 - \gamma) - a\gamma (w^*)^{(a+1/2)} / ((w^*)^a - 1)] / w_c, & w^* > 1 \end{cases} \quad (20)$$

where

$$\gamma = \exp(1/(1 - (w^*)^d)) \quad (21)$$

Likewise, the unloading normal stiffness k_n^U was derived by substituting Eqs. (3), (13) and (18) into Eq. (19):

$$k_n^U = \begin{cases} 3(w^*)^{1/2} f_c (1 + r^2/R_s^2)^{-1} / (2w_c), & 0 < w^* \leq 1 \\ 1.5 f_{\max} (w_{\max}^*)^b (1 + r^2/R_s^2)^{-1} (w^* - w_{\text{res}}^*)^{1.5(w_{\max}^*)^b - 1} / (w_c (w_{\max}^* - w_{\text{res}}^*)^{1.5(w_{\max}^*)^b}), & w^* > 1 \end{cases} \quad (22)$$

As assumed before, the asperities were in contact with each other independently. Then the loading and unloading normal pressure and stiffness of total contact surfaces, P and K_n , can be acquired by simply summing the components of the pressure and stiffness of single asperity pairs with the generalized formulas:

$$P = \sum_{g=1}^q |f_{n,g}(d)| / S \quad (23)$$

$$K_n = |\partial P / \partial d| = \sum_{g=1}^q |k_{n,g}(d)| / S \quad (24)$$

where $f_{n,g}(d)$ and $k_{n,g}(d)$ are the contact force and stiffness of the number g contact pair at surface separation d , q is the total number of contact pairs and S is the nominal contact area.

As mentioned above, the stiffness of contact surfaces was predicted with the proposed theoretical stiffness model in two steps. The first step was to get the normal stiffness of each single asperity contact with Eqs. (20) and (22), and the second step was to sum all the stiffness components as the stiffness of surface contact with Eq. (24). These were also the procedure to get the experimental values of the surface contact stiffness as shown in Section 4.

4. Experimental measurement and theoretical prediction of normal stiffness

In this section, two power-law hardening metallic materials were chosen to demonstrate the detailed method of experimental measurement and theoretical prediction of normal contact stiffness.

4.1. Experimental measurement procedure

The normal stiffness of contact surfaces was measured on the specimens compressed together in dry contact using the hydraulic jack (CRSM-50, Juding Inc., China), after the contact surfaces were cleaned by ultrasonic cleaning for 15 min in alcohol. Both the loading and unloading stiffness of contact surfaces K_n could be

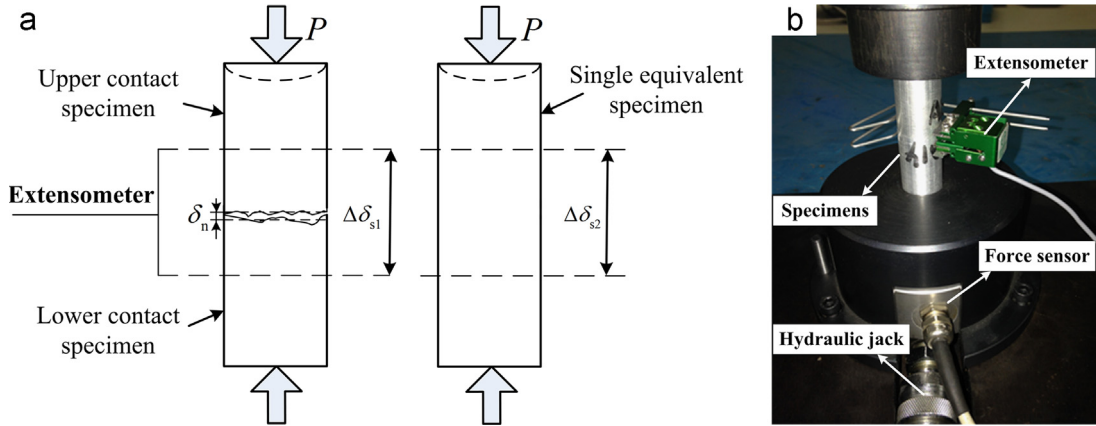


Fig. 5. Schematic diagram (a) and experimental setup (b) of normal stiffness measurement.

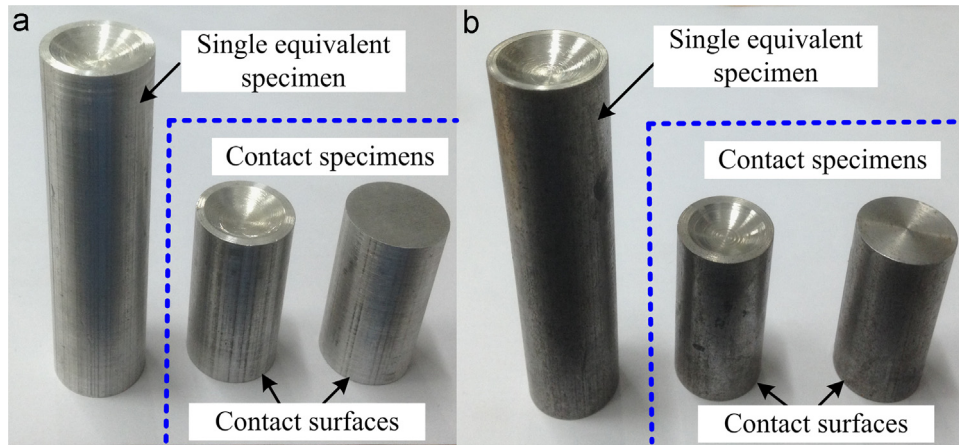


Fig. 6. Specimens of two materials for stiffness measurement, AlZn6CuMgZr aluminum alloy (a) and 18CrMo4 steel (b).

Table 1
Material parameters of specimens.

Specimen	Young's modulus E (GPa)		Yield strength Y_0 (MPa)		Poisson' ratio ν		Strain hardening exponent n	
	μ_E	σ_E	μ_{Y_0}	σ_{Y_0}	σ_ν	σ_ν	μ_n	σ_n
AlZn6CuMgZr aluminum alloy	71.7	1.21	528	2.3	0.33	0.004	0.21	0.010
18CrMo4 steel	197.6	2.87	469	3.7	0.29	0.003	0.15	0.007

derived indirectly with

$$K_n = |\partial P / \partial \delta_n| = |\partial (F_n / S) / \partial \delta_n| \quad (25)$$

where F_n is the normal contact force measured by the force sensor (K450, Lorenz-Messtechnik Co., Germany), δ_n is the change of the normal relative deformation of asperities obtained by the formula

$$\delta_n = |\Delta \delta_{s1} - \Delta \delta_{s2}| \quad (26)$$

where $\Delta \delta_{s1}$ and $\Delta \delta_{s2}$ are the relative deformation of the contact pair and the single equivalent specimen respectively. The different between δ_n here and d in Eq. 12 is that δ_n is equal to the change of d . The relative deformation was measured by the extensometer (Epsilon3442, Epsilon Co., USA). The measurement schematic diagram and the experiment setup are shown in Fig. 5. Five measurements were performed independently for each material to obtain the average results. To compare with the results predicted by the proposed model at different loads, the specimens were loaded in two sequential processes without any pause:

loading from 0 to 33.5 MPa and unloading to 3 MPa; then, loading from 3 MPa to 64 MPa and unloading to 3 MPa. The pressure on the specimens should not be removed completely to avoid the lateral motion of the surfaces.

As the specimens played an important role in both experimental measurement and theoretical prediction of normal stiffness, they are described in detail in the next section.

4.2. Specimen

AlZn6CuMgZr (ISO) aluminum alloy and 18CrMo4 (ISO) steel were chosen as two materials of the specimens. Five groups of specimens for each material with similar roughness were prepared using the same machining methods and same process parameters, to repeat the stiffness measurements. Each group contains a contact pair (including two short specimens) and a single equivalent specimen. The contrast experiments were carried out on the contact pair and the single equivalent specimen respectively to

eliminate the effect of the deformation of the solid material. The two types of cylindrical specimens were prepared with the sizes of $\phi 18 \text{ mm} \times 40 \text{ mm}$ and $\phi 18 \text{ mm} \times 80 \text{ mm}$ respectively (see Fig. 6). The upper specimen was loaded by a ball joint, with which the surfaces could be aligned to each other. The number of the specimens was 30, and 20 experiments in total were carried out.

The average roughness R_a of five groups for AlZn6CuMgZr aluminum alloy was $2.13 \mu\text{m}$ by grinding and the corresponding standard deviation was $0.14 \mu\text{m}$, while for 18CrMo4 steel the average R_a was $2.52 \mu\text{m}$ by turning whose standard deviation was $0.17 \mu\text{m}$. The average values μ and the corresponding standard deviation σ of material parameters such as Young's modulus E , yield strength Y_0 , Poisson's ratio ν , and strain hardening exponent n were gotten by the tensile tests, which are shown in Table 1.

4.3. Surface topography measurement and analysis

The engineering surfaces are generally large, and it is impractical to measure the whole surface topographies. Thus some test areas were chosen to represent the whole surface, which could consider the effect of the actual topographies efficiently. As Fig. 7 shows, eight test areas on each contact surface were selected evenly, and the size of each test area was $2 \text{ mm} \times 2 \text{ mm}$. The mating test areas were marked as couples such as A and A'. To make the mating test areas aligned before the experiment, each specimen in contact was marked with two signs at the same position of the edge of the cylindrical surface. When the two signs are aligned, it means the mating test areas are also aligned. The topographies were measured by white light interferometer (WYKO NT9300, Veeco Instruments Inc., USA) in VSI mode after the surfaces were cleaned by ultrasonic cleaning for 15 min in alcohol. The size of the scanned area of the white light interferometer was $640 \mu\text{m} \times 480 \mu\text{m}$, and thus each test area included several

scanned areas. The vertical and lateral resolutions were set as 0.1 nm and 975.85 nm respectively. Two typical topographies in one scanned area are illustrated in Fig. 8.

The topography data were obtained and the coordinates (x, y, z) of all points in test areas were stored. According to Eqs. (20) and (22), the radii and heights of the asperities and the tangential offset of two contact asperities are essential to calculate the stiffness of single asperity contact. Here (x, y, z, R_v) is defined as the "property parameters" of the asperity, where (x, y) is the location of an asperity, z and R_v are its height and radius of summit. The tangential offset r between asperity i and the mating asperity j can be obtained indirectly by

$$r = \sqrt{(x_i - x_j)^2 + (y_i - y_j)^2} \tag{27}$$

where (x_i, y_i) and (x_j, y_j) are the respective coordinates of the asperities i and j .

The primary work should be to identify the asperities and obtain their property parameters. Since the coordinates of all points were obtained, the asperity could be identified with the following procedure. First, locate the asperity vertices with the mathematical expression using MATLAB software:

$$z(i, j) \in \text{asperityvertices} \Leftrightarrow z(i, j) > z(u, v) \tag{28}$$

with $u = i - 2, i - 1, i, i + 1, i + 2$; $v = j - 2, j - 1, j, j + 1, j + 2$; and $u, v \neq i, j$.

Once an asperity vertex had been located, its heights could be obtained by the z -coordinate. The asperity densities η were determined by the vertex numbers in the corresponding nominal test areas. Secondly, the asperity was defined by its curvature. The asperity shape was fitted with an elliptic paraboloid with the coordinates of the five sequential points bordering the vertices in x - z and y - z planes respectively, namely nine points were used to describe one asperity. More than 85% of asperities on all test areas were fitted using this method with the adjusted R -square larger

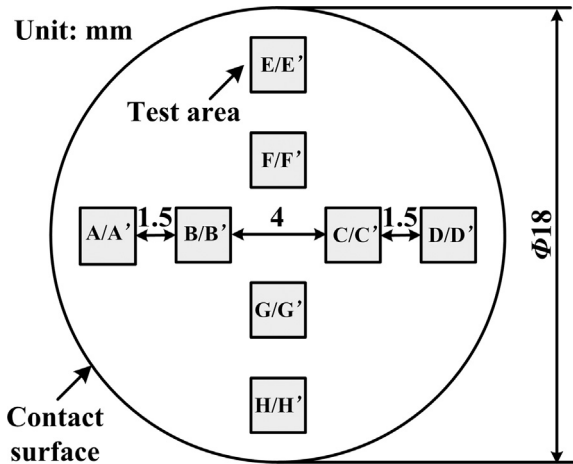


Fig. 7. Distribution of test areas on one contact surface.

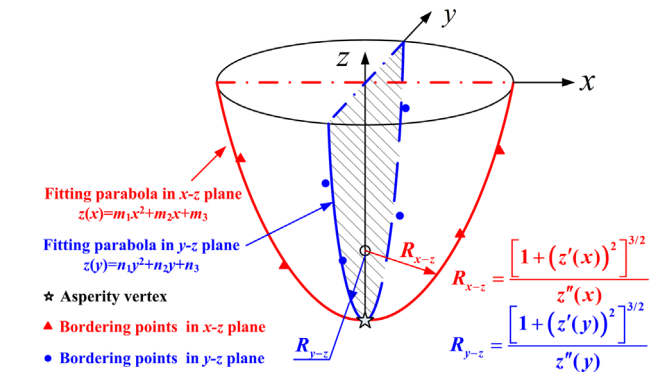


Fig. 9. Schematic of the algorithm to determine the asperity radii of summit in x - z plane and y - z plane.

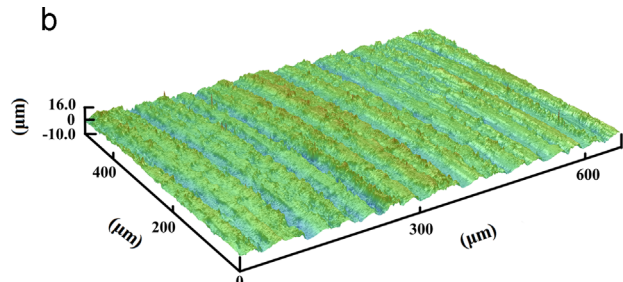
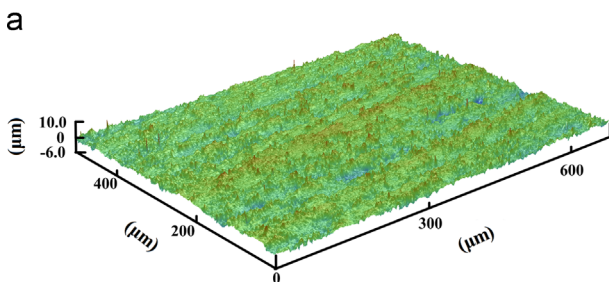


Fig. 8. Typical topographies in a scanned area ($S = 640 \mu\text{m} \times 480 \mu\text{m}$) of two materials, AlZn6CuMgZr aluminum alloy (a) and 18CrMo4 steel (b).

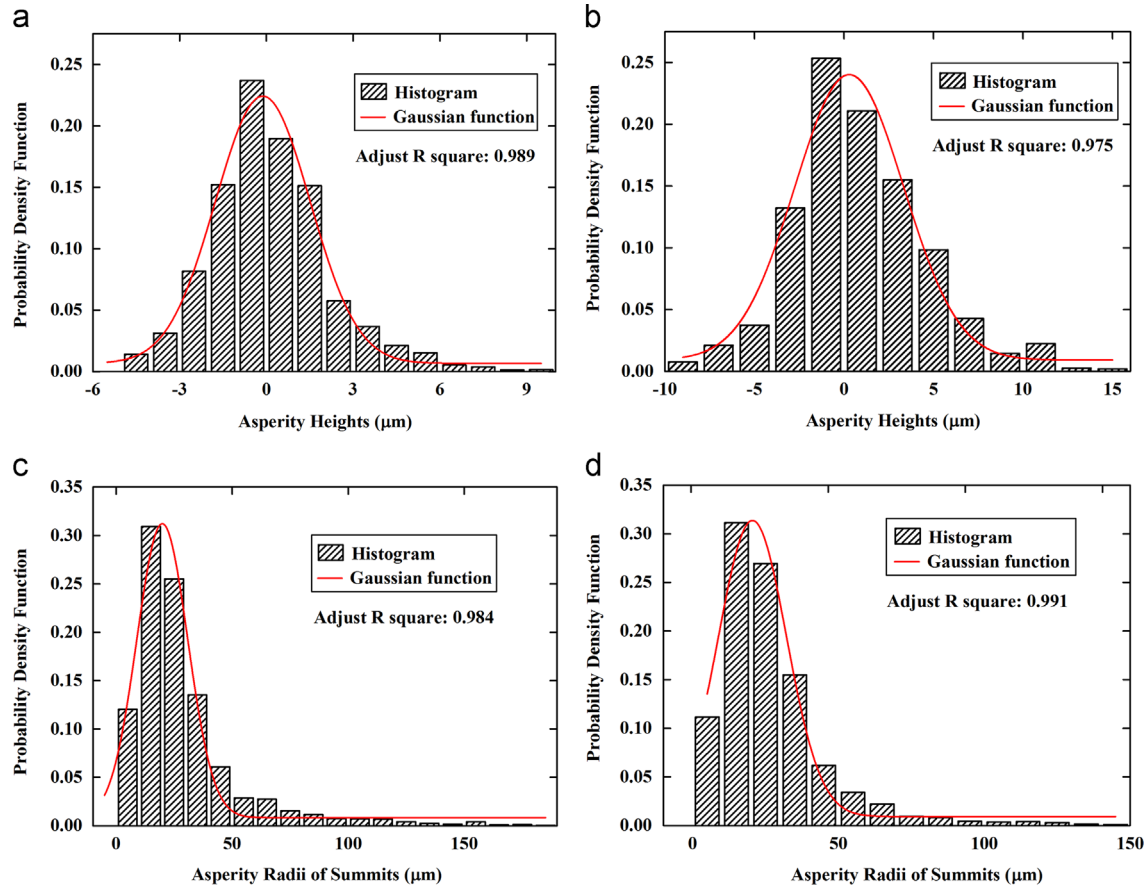


Fig. 10. General statistical distribution of asperity heights and radii of summits based on 8 test areas in one typical contact surface ($S = \pi \cdot 9^2 \text{ mm}^2$): distribution of asperity heights of AlZn6CuMgZr aluminum alloy (a) and 18CrMo4 steel (b); distribution of asperity radii of summits of AlZn6CuMgZr aluminum alloy (c) and 18CrMo4 steel (d).

Table 2

General parameters of contact surfaces ($S = \pi \cdot 9^2 \text{ mm}^2$).

Specimen		Radius of summit R (μm)		Asperity height z (μm)		Asperity density η (/mm ²)	
		μ_R	σ_R	μ_z	σ_z	μ_η	σ_η
AlZn6CuMgZr aluminum alloy	Upper	19.87	21.94	-0.13	3.27	38,216	446
	Lower	17.43	19.76	-0.11	2.96	37,548	435
18CrMo4 steel	Upper	20.52	23.37	0.29	6.08	39,661	457
	Lower	21.64	25.12	0.33	6.32	40,727	482

than 0.90, which means the fits were good. The radii at the vertices in $x-z$ plane, R_{x-z} and in $y-z$ plane, R_{y-z} were acquired as shown in Fig. 9. The equivalent radii at the vertices R_v , i.e. the radii of summits in Fig. 4, were then obtained with the radii R_{x-z} and R_{y-z} .

$$1/R_v = \sqrt{(1/R_{x-z})(1/R_{y-z})} \quad (29)$$

The property parameters of all asperities were obtained with the method above.

To show the geometric characteristics of the asperities in detail, the Gaussian distributions of asperity heights and that of radii of summits were produced. The probability density function $\varphi(\xi)$ of the Gaussian distribution is expressed as

$$\varphi(\xi) = \exp(-(\mu - \xi)^2 / (2\sigma^2)) / (\sigma\sqrt{2\pi}) \quad (30)$$

For the distribution of asperity heights, μ and σ were replaced with μ_z and σ_z to represent the average value and the standard deviation of asperity heights. Note that the reference plane of the heights was defined as the mean plane of the asperity heights, just

Table 3

Values of critical interference, critical force and plasticity index.

Specimen		Critical interference w_c (μm)	Critical force f_c (mN)	Plasticity index ψ
AlZn6CuMgZr aluminum alloy	Upper	0.0052	0.192	25.08
	Lower	0.0047	0.148	25.10
18CrMo4 steel	Upper	0.0053	0.162	24.84
	Lower	0.0055	0.180	23.20

as many researchers defined. While for the distribution of the radii of summit, μ and σ were replaced with μ_R and σ_R to represent the average value and the standard deviation of asperity radii. The general statistic distributions in one contact surface are illustrated in Fig. 10. All the adjusted R -squares are over 0.90 which indicates the statistical distribution of radii and heights could be fitted well with Gaussian function. Moreover, the statistics of the asperity density η was also carried on to obtain the average values μ_η and

the corresponding standard deviation σ_η . All general parameters averaged by 8 test areas in one contact surface are shown in Table 2.

Note that these parameters in Table 2 were just used to show the topography characteristics of contact surfaces, rather than to generate asperities. The detailed method to generate asperities with actual geometrical parameters was presented in Section 4.4.

The Greenwood and Williamson model [12] introduced the plasticity index ψ to measure the contact status combining the material and topographic properties of the solids. The index ψ is calculated by the expression $\psi = (w_c/\sigma_z)^{-0.5}$. If ψ is less than 0.6, the elastic contact is dominated, while if ψ exceeds 1.0, the plastic contact happens even at small loads and the elastic–plastic property should be considered. The values of critical interference

w_c and critical force f_c were calculated using the Eqs. (3) and (2) in which R was replaced with the average radius of summit μ_R in Table 2. The values of w_c and f_c for two materials are listed in Table 3.

It can be seen from Table 3, the values of ψ for the specimens in this work are all larger than 1.0, which means the elastic–plastic formulations in Section 2 can be adopted.

4.4. Approach of normal stiffness prediction

The loading and unloading normal stiffness of each couple of test areas was calculated following the procedure as illustrated in Fig. 11. The surface topography was measured and analyzed at first and the property parameters of asperities were obtained and stored. Then the asperity was generated with the actual height and radius at the actual position determined by the property parameters. This algorithm was iterated N and M times for the contact test areas, where N is the asperities numbers in one area and M is that in the other area. Since all asperities on test areas were generated with the deterministic measured parameters, the stiffness model was actually a deterministic model. The interference w_1 was obtained at the given separation of contact surfaces d . As d between two test areas (e.g. A and A') becomes smaller, w_1 increases from 0 to larger values. When w_1 first becomes larger than 0, it can be said the contact occurs, namely it is the origin for the contact description. Then the loading and unloading stiffness of single asperity contact pair were determined by Eqs. (20) and (22). Iterate this calculation from $d=0$ to $d=d_{max}$, where the maximum separations d_{max} equals to the sum of the maximum asperity heights of two contacting surfaces. Finally the normal stiffness of the whole contact surfaces was obtained by summing the components of each asperity contact pair with Eq. (24). All above processes were carried out with MATLAB 7.0.

5. Results and discussions

The experimental data of the normal pressure versus deformation and the fitting curves are shown in Fig. 12. The initial loading curve from 0 to 64 MPa was smooth and continuous though it was interrupted by the unloading process. It indicates the elastic and plastic deformation of the asperities at their first contact. Owing to the existence of plastic deformation, the subsequent unloading curve was different from the loading curve due to the hysteresis. It shows the relation of the decreasing pressure and the recovered elastic deformation. During the second loading, if the pressure is

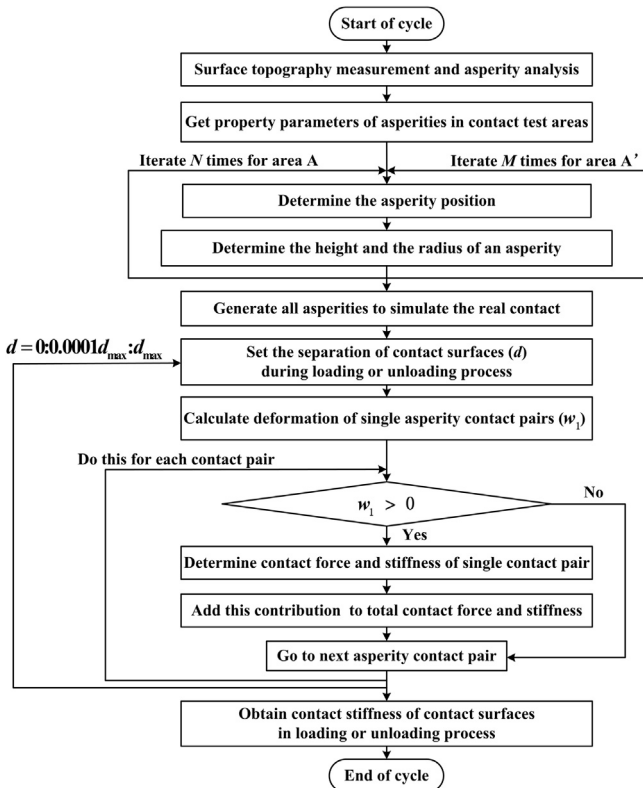


Fig. 11. Procedure for the determination of the loading and unloading normal stiffness of contact surfaces.

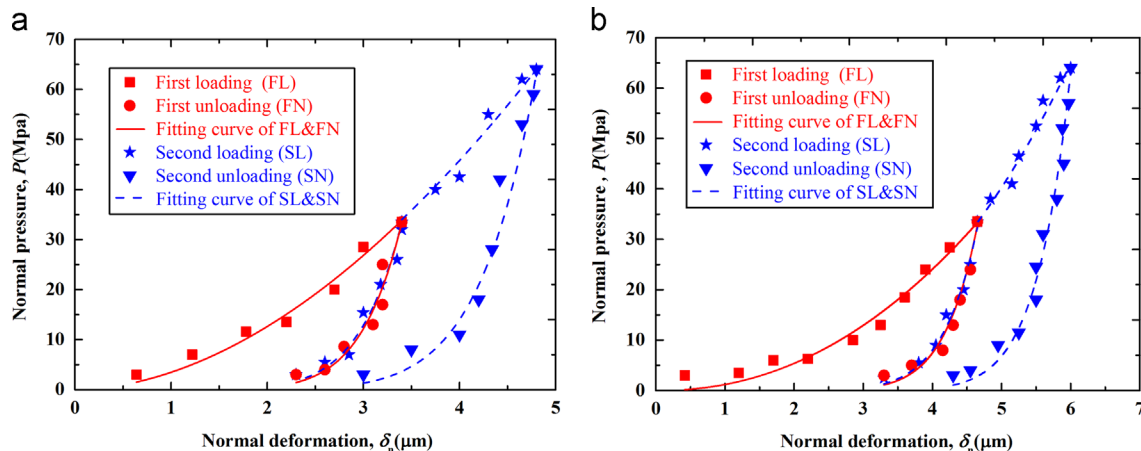


Fig. 12. Experimental data of normal pressure P versus normal deformation δ_n and the corresponding fitting curves in two loading–unloading process for two materials, AlZn6CuMgZr aluminum alloy (a) and 18CrMo4 steel (b).

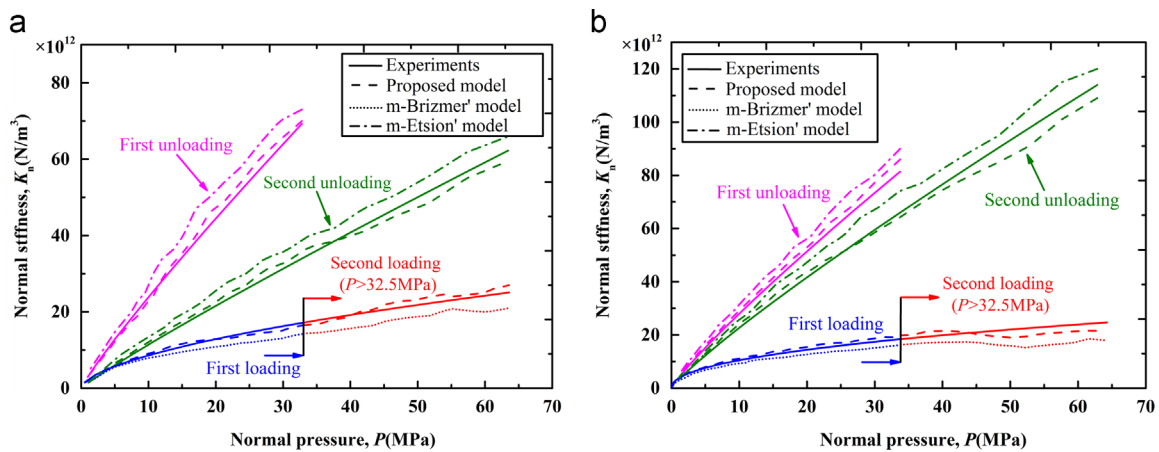


Fig. 13. Comparison of normal stiffness predicted by different stiffness models and experimental results of AlZn6CuMgZr aluminum alloy (a) and 18CrMo4 steel (b). In first loading and second loading ($P > 32.5$ MPa) process, the proposed stiffness model was compared with the m-Brizmer's model and the experimental results. While in first and second unloading process, the proposed stiffness model was compared with the m-Etsion's model and the experiments.

under 33.5 MPa, the pressure–deformation relation accords with the first unloading curve because only elastic deformation occurs in this process; while if the pressure exceeds 33.5 MPa, the additional plastic deformation occurs and the curve continues the first loading curve until the specimens are unloaded again.

The normal stiffness predicted by the proposed model was compared with the experimental data as shown in Fig. 13. In addition, the stiffness obtained by another two existing stiffness models was also plotted for comparison. One was based on the contact model of single asperity pair given by Brizmer et al. [34] during loading, while the other was based on the contact model given by Etsion et al. [27] during unloading. Both models calculated the stiffness of contact surfaces considering the effect of the actual topography with the method presented in Section 4. These two stiffness models were marked as m-Brizmer's model and m-Etsion's model respectively. As shown in Fig. 13, at higher pressure, more and more asperities are in contact, resulting in a higher normal stiffness. Besides, the unloading stiffness is much higher than the loading stiffness in the elastic–plastic regime. This is because in the loading process, both the elastic and plastic deformation occurs as the pressure increases. While in the unloading process, only the elastic deformation recovers, leading to the pressure decreasing more quickly as the deformation changes. Moreover, in two loading processes, the proposed stiffness model is closer to the experiments than the m-Brizmer's model. This occurs because the Brizmer's model assumes the contact materials as linear hardening with 2% tangent modulus. By comparison, the proposed model is based on the power-law hardening assumption which is more accurate to describe the real hardening behavior of these materials. Similarly in unloading process, the proposed model is also closer to the experiments than the m-Etsion's model. The reason is that the Etsion's model is built on the assumptions of 2% tangent modulus hardening and the frictionless condition, which are less real than the proposed model.

The errors λ between the stiffness predicted by the stiffness models $K_{n,model}$ and that obtained by the experiments $K_{n,experiment}$ were calculated by

$$\lambda = |(K_{n,model} - K_{n,experiment}) / K_{n,experiment}| \times 100\% \quad (31)$$

For the loading process, the maximum error between the stiffness predicted by m-Brizmer's model and the experiments results could reach larger than 30%. While for the unloading process, the maximum error between the stiffness predicted by m-Etsion's model and the experiments results were larger than 15%. By comparison, the proposed model is in good accordance with the

experiments due to the errors less than 10%, which depicts the proposed model is quite accurate. The errors might be caused by the neglect of the effect of the asperity interaction. This effect could be considered with the substrate deformation caused by the asperity contact. Thus the deformation used to calculate the stiffness should include two parts: the asperity deformation and the substrate deformation. The contact force should be adjusted due to the substrate deformation. Then with the adjusted contact force and deformation, the stiffness could be calculated including the effect of asperity interaction. This will be finished in the further work.

6. Conclusions

A normal stiffness model for the power-law hardening surfaces considering the actual surface topography during loading and unloading process was presented and validated by the experiments on AlZn6CuMgZr aluminum alloy and 18CrMo4 steel, with stiffness errors less than 10%. Two other stiffness models with the assumptions of 2% tangent modulus hardening or the frictionless contact condition were also compared with the experiments in loading and unloading processes respectively. It showed this proposed model was more accurate and appropriate to predict the loading and unloading normal stiffness of contact surfaces for the power-law hardening materials.

Acknowledgment

This work was supported by the National Major Science and Technology Project High-end CNC Machine Tools and Basic Manufacturing Equipments (Grant no. 2012ZX04006-011) and the Taishan Scholar Program Foundation of Shandong.

The authors are greatly thankful to Mr. Jinhua Zhang from State Key Lab for Manufacturing System Engineering, Xi'an Jiaotong University for their technical assistance in experiment apparatus.

References

- [1] Wu L, Golinval JC, Noels L. A micro-model for elasto-plastic adhesive-contact in micro-switches: application to cyclic loading. *Tribol Int* 2013;57:137–46.
- [2] Vakis AI, Polycarpou AA. Head-disk interface nanotribology for Tbit/inch² recording densities: near-contact and contact recording. *J Phys D Appl Phys* 2010;43:225301.
- [3] Fu RJ, Choe SY, Jackson RL, Flowers GT, Bozack MJ, Zhong L, et al. Vibration-induced changes in the contact resistance of high power electrical connectors for hybrid vehicles. *IEEE Trans Compon Packag Manuf Technol* 2012;2:185–93.

- [4] Qin WJ, Guan CY. An investigation of contact stresses and crack initiation in spur gears based on finite element dynamics analysis. *Int J Mech Sci* 2014;83:96–103.
- [5] Ben-David O, Rubinstein SM, Fineberg J. Slip–stick and the evolution of frictional strength. *Nature* 2010;463:76–9.
- [6] Smerdova O, Mazuyer D, Cayer-Barrioz J. Links between energy dissipation and wear mechanisms in solid epoxy/epoxy sliding contact. *Tribol Int* 2014;77:148–59.
- [7] Xie L, He PF, Zhou J, Lacks DJ. Correlation of contact deformation with contact electrification of identical materials. *J Phys D Appl Phys* 2014;47:215501.
- [8] Mulvihill DM, Brunskill H, Kartal ME, Dwyer-Joyce RS, Nowell D. A Comparison of contact stiffness measurements obtained by the digital image correlation and ultrasound techniques. *Exp Mech* 2013;53:1245–63.
- [9] Kartal ME, Mulvihill DM, Nowell D, Hills DA. Measurements of pressure and area dependent tangential contact stiffness between rough surfaces using digital image correlation. *Tribol Int* 2011;44:1188–98.
- [10] Boscolo M, Banerjee JR. Dynamic stiffness formulation for composite Mindlin plates for exact modal analysis of structures. Part II: results and applications. *Comput Struct* 2012;96:74–83.
- [11] Giraudeau A, Pierron F, Guo B. An alternative to modal analysis for material stiffness and damping identification from vibrating plates. *J Sound Vib* 2010;329:1653–72.
- [12] Greenwood JA, Williamson J. Contact of nominally flat surfaces. *Proc R Soc Lond: A* 1966;295:300–19.
- [13] Greenwood JA, Tripp JH. The contact of two nominally flat rough surfaces. *Proc Inst Mech Eng* 1970;185:625–33.
- [14] Chang WR, Etsion I, BOGY DB. An elastic–plastic model for the contact of rough surfaces. *J Tribol* 1987;109:257–63.
- [15] Zhao Y, Maietta DM, Chang L. An asperity microcontact model incorporating the transition from elastic deformation to fully plastic flow. *J Tribol* 2000;122:86–93.
- [16] Chang L. A deterministic model for line-contact partial elasto-hydrodynamic lubrication. *Tribol Int* 1995;28:75–84.
- [17] Jackson RL, Green I. On the modeling of elastic contact between rough surfaces. *Tribol Trans* 2011;54:300–14.
- [18] Mandelbrot BB. *The fractal geometry of nature*. London: Macmillan; 1983.
- [19] Miao X, Huang X. A complete contact model of a fractal rough surface. *Wear* 2014;309:146–51.
- [20] Goedecke A, Jackson RL, Mock R. A fractal expansion of a three dimensional elastic–plastic multi-scale rough surface contact model. *Tribol Int* 2013;59:230–9.
- [21] Goerke D, Willner K. Normal contact of fractal surfaces—experimental and numerical investigations. *Wear* 2008;264:589–98.
- [22] Kogut L, Etsion I. Elastic–plastic contact analysis of a sphere and a rigid flat. *ASME J Appl Mech* 2002;69:657–62.
- [23] Jackson RL, Green I. A finite element study of elasto-plastic hemispherical contact against a rigid flat. *ASME J Tribol* 2005;127:343–54.
- [24] Shankar S, Mayuram MM. Effect of strain hardening in elastic–plastic transition behavior in a hemisphere in contact with a rigid flat. *Int J Solids Struct* 2008;45:3009–20.
- [25] Toler BF, Jr RA Coutu, McBride JW. A review of micro-contact physics for microelectromechanical systems (MEMS) metal contact switches. *J Micro-mech Microeng* 2013;23:103001.
- [26] Peng W, Bhushan B. Transient analysis of sliding contact of layered elastic/plastic solids with rough surfaces. *Microsyst Technol* 2003;9:340–5.
- [27] Etsion I, Kligerman Y, Kadin Y. Unloading of an elastic–plastic loaded spherical contact. *Int J Solids Struct* 2005;42:3716–29.
- [28] Kadin Y, Kligerman Y, Etsion I. Loading–unloading of an elastic–plastic adhesive spherical microcontact. *J Colloid Interface Sci* 2008;321:242–50.
- [29] Jackson R, Chusoipin I, Green I. A finite element study of the residual stress and deformation in hemispherical contacts. *ASME J Tribol* 2005;127:484–93.
- [30] Jackson RL, Green I, Marghitu DB. Predicting the coefficient of restitution of impacting elastic–perfectly plastic spheres. *Nonlinear Dyn* 2010;60:217–29.
- [31] McGuiggan PM. Stick slip contact mechanics between dissimilar materials: effect of charging and large friction. *Langmuir* 2008;24:3970–6.
- [32] Ovcharenko A, Halperin G, Etsion I. In situ and real-time optical investigation of junction growth in spherical elastic–plastic contact. *Wear* 2008;264:1043–50.
- [33] Brizmer V, Kligerman Y, Etsion I. The effect of contact conditions and material properties on the elasticity terminus of a spherical contact. *Int J Solids Struct* 2006;43:5736–49.
- [34] Brizmer V, Zait Y, Kligerman Y, Etsion I. The effect of contact conditions and material properties on elastic–plastic spherical contact. *J Mech Mater Struct* 2006;1:865–79.
- [35] Ovcharenko A, Halperin G, Verberne G, Etsion I. In situ investigation of the contact area in elastic–plastic spherical contact during loading–unloading. *Tribol Lett* 2007;25:153–60.
- [36] Zait Y, Kligerman Y, Etsion I. Unloading of an elastic–plastic spherical contact under stick contact condition. *Int J Solids Struct* 2010;47:990–7.
- [37] Ramberg W, Osgood WR. Description of stress–strain curves by three parameters. NACA technical note no. 902; 1943; 1–28.
- [38] Olsson E, Larsson PL. On force–displacement relations at contact between elastic–plastic adhesive bodies. *J Mech Phys Solids* 2013;61:1185–201.
- [39] Zhao JH, Nagao S, Zhang ZL. Loading and unloading of a spherical contact: from elastic to elastic–perfectly plastic materials. *Int J Mech Sci* 2012;56:70–6.
- [40] Sepehri A, Farhang K. On elastic interaction of nominally flat rough surfaces. *J Tribol* 2008;130:011014.
- [41] Kogut L, Etsion I. A finite element based elastic–plastic model for the contact of rough surfaces. *Tribol Trans* 2003;46:383–90.
- [42] Rostami A, Jackson RL. Predictions of the average surface separation and stiffness between contacting elastic and elastic–plastic sinusoidal surfaces. *Proc IMechE Part J: J Eng Tribol* 2013;227:1376–85.
- [43] Chandrasekar S, Eriten M, Polycarpou AA. An improved model of asperity interaction in normal contact of rough surfaces. *J Appl Mech* 2013;80:011025.
- [44] Christensen PW, Klarbring A, Pang JS, Strömberg N. Formulation and comparison of algorithms for frictional contact problems. *Int J Numer Methods Eng* 1998;42:145–73.
- [45] Johnson KL. *Contact mechanics*. Cambridge: Cambridge University Press; 1995.